Spatiotemporal Dynamics of Oscillatory Cellular Patterns in Three-Dimensional Directional Solidification

N. Bergeon,[1,*] D. Tourret,[2,†] L. Chen,[1] J.-M. Debierre,[1] R. Guérin,[1] A. Ramirez,[1] B. Billia,[1] A. Karma,[2] and R. Trivedi[3]

[1]*Institut Matériaux Microélectronique Nanosciences de Provence, Aix-Marseille Université and CNRS UMR 7334, Campus Saint-Jérôme, Case 142, 13397 Marseille Cedex 20, France*

[2]*Department of Physics and Center for Interdisciplinary Research on Complex Systems, Northeastern University, Boston, Massachusetts 02115, USA*

[3]*Department of Materials Science and Engineering, Iowa State University, Ames, Iowa 50010, USA*

(Received 25 February 2013; published 28 May 2013)

We report results of directional solidification experiments conducted on board the International Space Station and quantitative phase-field modeling of those experiments. The experiments image for the first time *in situ* the spatially extended dynamics of three-dimensional cellular array patterns formed under microgravity conditions where fluid flow is suppressed. Experiments and phase-field simulations reveal the existence of oscillatory breathing modes with time periods of several 10's of minutes. Oscillating cells are usually noncoherent due to array disorder, with the exception of small areas where the array structure is regular and stable.

DOI: 10.1103/PhysRevLett.110.226102 PACS numbers: 68.08.−p, 05.70.Ln, 64.70.D−, 81.30.Fb

Directional solidification of binary alloys leads to the formation of a rich variety of nonequilibrium interface patterns that have been widely studied as examples of pattern formation [1] as well as for their metallurgical relevance [2,3]. Common solidification patterns are spatially extended arrays of cells or dendrites that form above the onset of morphological instability. While extensive experimental and theoretical work during the past several decades has yielded basic insights into those patterns [3], their dynamics in three-dimensions (3D) still remains poorly characterized and understood. In particular, the third dimension brings the crucial problem of understanding the spatiotemporal organization of space-filling growth patterns, as highlighted by Thomson [4] and explored since then in various physical and biological systems [5,6]. Transparent organic alloys have been extensively used to image *in situ* the dynamics of the solid-liquid interface [7]. However, fluid convection on Earth leads to large-scale inhomogeneities of temperature and composition in bulk samples. Those inhomogeneities strongly influence the microstructure [8,9] and impede the probing of spatially extended pattern dynamics under controlled diffusive growth conditions with constant growth velocity (V), temperature gradient (G), and alloy composition (c_∞). Hence, experimental studies of interface dynamics have been restricted primarily to thin samples where fluid flow is eliminated [10–15]. In addition, computational modeling of 3D patterns has remained challenging due to the several orders of magnitude disparity between capillary and transport scales.

In this Letter, we report the first live observation of breathing oscillations of spatially extended 3D cellular arrays obtained by imaging *in situ* the interface dynamics under microgravity conditions where fluid flow is suppressed. Spatiotemporal coherence of cellular arrays may thus be characterized in relation with ordering of the cellular array structure. Breathing modes are generic secondary oscillatory instabilities of spatially modulated interface patterns [16]. They have been experimentally and theoretically studied in 2D for both cellular [12,14,17,18] and two-phase eutectic [19] interfaces. They have also been theoretically predicted for 3D cellular growth [20,21]. While those previous experiments exhibited global spatiotemporal coherence over large domains, the present microgravity experiments reveal a variety of 3D breathing modes with limited spatiotemporal coherence. Massively parallel 3D phase-field simulations, which access length and time scales of millimeters and hours, respectively, allow us to recover salient features of breathing modes and make quantitative comparisons with *in situ* observations that yield further insights into their dynamics.

Experiments were conducted on board the International Space Station in the Directional Solidification Insert developed by the French space agency CNES in the frame of the DEvice for the study of Critical LIquids and Crystallization (DECLIC) project and dedicated to *in situ* and real time characterization of the dynamical selection of the solid-liquid interface morphology on bulk transparent samples. A succinonitrile-camphor alloy was elaborated by adding $c_\infty = 0.24$ wt% camphor to pure succinonitrile supplied by the National Aeronautics and Space Administration. The alloy preparation and crucible filling were carefully realized under vacuum in order to avoid humidity contamination. The cylindrical crucible, which is sealed and inserted inside the Bridgman furnace, has an inner diameter of 1 cm and a length that enables ~10 cm of solidification, thus allowing the study of the whole development of extended cellular patterns from their initial formation to the steady state. The crucible is equipped with a flat glass window at the bottom and a lens immersed in the melt at the top. We take advantage of the complete axial transparency of the alloy to image a top view of the interface on a CCD camera. A complete description of the experimental setup and process appears in Refs. [22,23]. The physical parameters of the alloy are the solute partition coefficient $k = 0.21$, liquidus slope $m = -1.365$ K/wt%, Gibbs-Thomson coefficient $\Gamma = 6.48 \times 10^{-2}$ K/μm, anisotropy $\epsilon_4 = 0.007$ of the solid-liquid interface tension, and liquid solute diffusivity $D = 270$ μm^2/s (see, e.g., Refs. [24,25]).

The successive campaigns of experiments explored a wide range of growth conditions. We focus here on a temperature gradient ($G = 28$ K/cm) and a velocity range ($V = 0.5$–1.5 μm/s) for which oscillatory modes were observed. Oscillations affect small regions of the cell array when $V = 0.5$ μm/s, whereas the whole pattern oscillates for $V = 1.0$ μm/s (see video "Fig1a_Experiment_FullArray.avi" of the Supplemental Material [26]), and breathing ceases in the final stage of cellular growth at $V = 1.5$ μm/s. On the top view images, the oscillating cells are characterized by a periodic variation of their cross-sectional area $A(t)$ in a plane perpendicular to the growth direction [bright area in Fig. 1(a)]. The interferometry measurements performed during the experiments and phase-field simulations show that oscillations occur both in the vertical z direction, and in the (x, y) plane, so that both the tip position $z_{\text{tip}}(t)$ and the cell area $A(t)$ are oscillating functions of time t. Since the center-to-center distances remain constant, grooves oscillate laterally. The amplitude of $A(t)$ may either stay constant or increase, in which case cells eventually split into two cells, then one of these two cells usually oversteps the other and oscillation resumes. This represents a major difference with experiments in thin samples where tip splitting was observed to inhibit oscillations and rather induce a transition to a doublet structure [14].

We studied the distribution of the oscillation phase of a large group of cells in order to assess spatiotemporal coherence [26]. The distribution of phases on the unit circle shown in Fig. 1(b) reveals a large scatter of phases, therefore highlighting the absence of global coherence of oscillations, unlike in thin-sample experiments [14]. Most generally, adjacent cells do not present particular phase relation. This lack of coherence is related to the intrinsic short-range order of extended 3D patterns [see FFT in Fig. 1(a)] comparable to liquid structures, with numerous topological defects (number of nearest neighbors ≠ 6).

We generically observed the synchronization of neighboring cells in areas where local spatial ordering was maintained long enough, e.g., inside the two squares in Fig. 1(a) that display hexagonal and square ordering, respectively. The variations of $A(t)$ for the hexagonal pattern are represented in Fig. 2(a). The cells are organized as three sublattices that oscillate with the same period and a

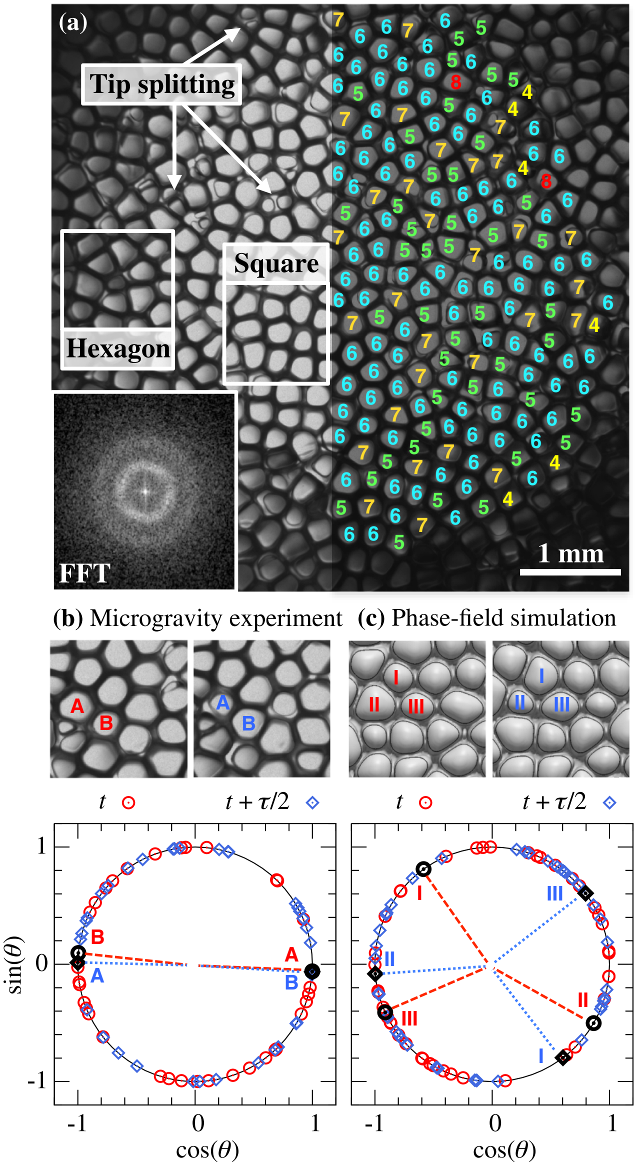

(b) Microgravity experiment (c) Phase-field simulation

FIG. 1 (color online). Spatially extended breathing cellular pattern observed from the liquid side in an experiment with $V = 1$ μm/s and $G = 28$ K/cm. A top view of a cellular array is shown in (a). The high spatial disorder of the array is highlighted by both the ring-shaped fast Fourier transform (FFT) of the image (inset) and the large number of array defects (the number of nearest neighbors of each cell is indicated on the right-hand side). All cells oscillate with nearly the same period but different phases. The phases (θ) are plotted on the unit circle on the lower diagrams at two times half a period ($\tau/2$) apart with different colors and symbols, for the experiment (b) and the simulation (c). The large scatter of phases indicates absence of global coherence of oscillations. In disordered regions, temporary synchronization between first-neighbor cells appears in both experiment and simulation, either with phase opposition [tagged cells in (b)], or with $\pm 2\pi/3$ phase shift [tagged cells in (c)], which correspond to the basic breathing modes. We provide the detailed image processing procedures to extract $A(t)$ for both experiments and simulations, as well as videos of the oscillatory patterns in the joint Supplemental Material [26].

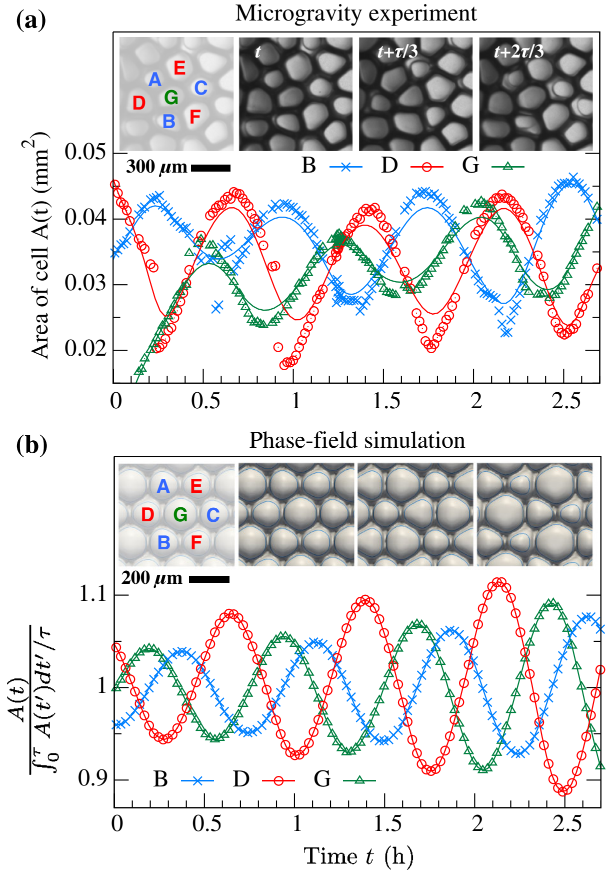

FIG. 2 (color online). Short-range correlation of hexagonal patterns at $V = 1$ μm/s and $G = 28$ K/cm. Inside the "hexagon" region of Fig. 1(a), three groups of cells oscillate coherently with a mutual phase difference of $\pm 2\pi/3$, as shown in (a). The phase-field simulation in (b) reproduces this coherent oscillation with a remarkably similar period.

phase shift of $\pm 2\pi/3$. Cells A, B, and C oscillate in phase; D, E, and F also oscillate in phase but with a $-2\pi/3$ phase shift with respect to the first group, while the central cell G oscillates with a $+2\pi/3$ phase shift with respect to the first group. A qualitatively similar $\pm 2\pi/3$ mode was found in previous numerical studies, albeit in the high velocity limit [20] or with a two-sided phase-field model [21]. We also observed the mode with π out of phase oscillations within a local square lattice ordering [e.g., "square" area in Fig. 1(a)] with the two sublattices of a checkerboard oscillating in phase opposition. However, those breathing modes lead to a short-range phase coherence that does not extend beyond neighboring cells.

Even though phase locking is limited to sparse ordered regions, the oscillation period τ is largely insensitive to the degree of phase coherence and thus remarkably uniform throughout the entire array. This period is plotted in Fig. 3 as a function of V and is reasonably well fitted by the power law $\tau = KV^{-3/2}$. The exponent and prefactor are both similar to those found for breathing modes in confined 3D experiments [14], despite different alloys and geometries. In thin samples, confinement imposes cell arrangement in a row. Yet, for sample thickness above ~25 μm, tip shapes are no longer ribbonlike (2D) but actually 3D [27]. In both cases, interactions are limited to first-neighbor spacing since the Péclet number $\mathrm{Pe} = \Lambda V/D$ with Λ the cell spacing is of order unity ($0.5 < \mathrm{Pe} < 1.5$ in our experiments). This very likely explains the similar power law exponent. Lacking experimental data for other alloys, a possible interpretation is that the agreement on the prefactor is related to the nature of the solvent (succinonitrile in both cases).

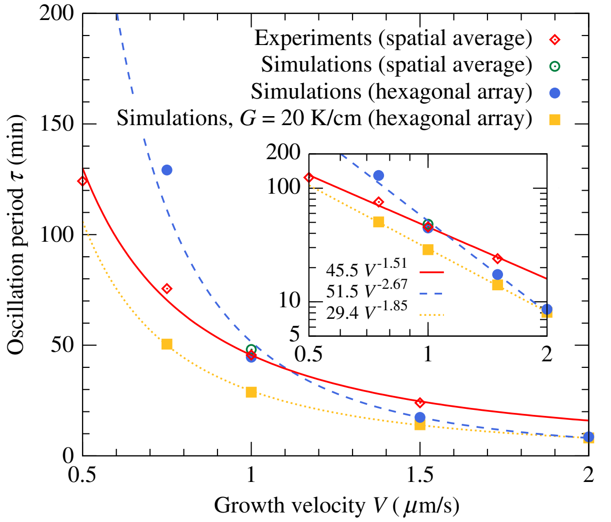

FIG. 3 (color online). Oscillation period vs growth velocity for $G = 28$ K/cm, as well as for a different set of parameters ($D = 230$ μm^2/s, $k = 0.2$, $G = 20$ K/cm) that has a lower critical velocity $V_c \approx 0.35$ μm/s (see Ref. [26]).

To gain further insights into breathing modes, we carried out 3D phase-field simulations using an established quantitative approach for binary alloys [27–30]. This approach renders accessible computations with local equilibrium at the interface and a diffuse interface thickness W much larger than the microscopic capillary length $d_0 = \Gamma/[mc_\infty(1 - 1/k)]$ (e.g., $W = 85$ d_0 for the present parameters at $V = 1$ μm/s). We performed the simulations for the physical parameters of the succinonitrile-camphor alloy given above (see complete details of the computational model, parameters, and procedures in the Supplemental Material [26]).

We carried out a first series of simulations in order to investigate the spatially extended dynamics of cellular arrays. Those simulations used large rectangular domains with periodic boundary conditions perpendicular to the growth direction and tracked the entire transient recoil and destabilization of an initially planar interface. Those simulations produced a similar oscillatory behavior of cellular arrays as in the experiments with a mix of short-range coherent breathing modes and globally incoherent oscillations. This is illustrated in Fig. 1(c) where the phases

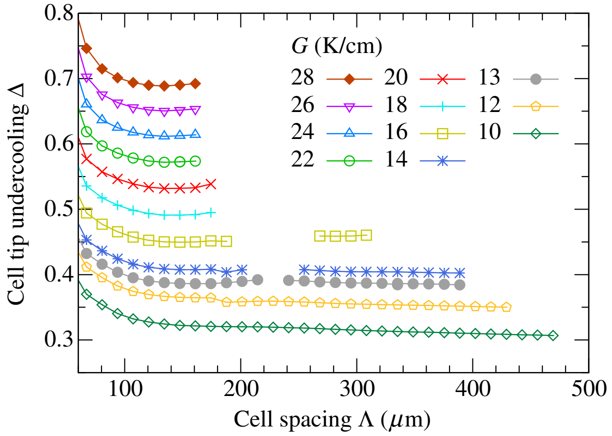

FIG. 4 (color online). Phase-field predictions of steady-state branches of hexagonal cellular arrays for $V = 1\ \mu\text{m/s}$ where Δ is the cell tip undercooling below the liquidus temperature normalized by the freezing range $mc_\infty(1\text{–}1/k)$.

of a large group of cells are scattered around the unit circle but some neighbor cells with local hexagonal ordering display short-range coherence with a $\pm 2\pi/3$ mode (tagged points). As in the experiment, the oscillation period is uniform over the array, and its average value $\tau \approx 48.1$ min for $V = 1\ \mu\text{m/s}$ is consistent with the experimental period $\tau \approx 45.6$ min.

We performed an additional series of simulations that enforced hexagonal ordering in order to investigate the range of existence of oscillatory modes as a function of control parameters and cell spacing. First, we simulated the steady-state growth of one quarter of a cell that was part of a hexagonal array by using appropriate periodic boundary conditions [26]. The cell spacing was thus fixed by the size of the simulation box. The results of such simulations with varying box size show that steady-state solutions only exist over a limited range of cell spacings, as shown in Fig. 4. At low G, the hexagonal branch of steady-state solutions spans continuously a broad range of spacings. A gap in this branch, previously found for a different alloy and control parameters [27], appears for intermediate values of G, and the rightmost branch disappears at even higher G. Next, steady-state cells were repeated in a larger simulation box (3/2 of a cell) with imposed hexagonal symmetry to study the breathing modes (see details in Ref. [26]). The results of those simulations show that cell spacings towards the end of the main (leftmost) branch display breathing oscillations when a gap is present, and at higher G, while cells are stable when the gap closed at lower G. Those modes are temporally sustained for an extremely narrow range of spacing. The oscillations generally increase in amplitude over a few periods ending in cell splitting, as seen experimentally. Figure 2(b) shows a sustained breathing mode that displays a period of $\tau = 44.6$ mn, which is close to the spatial average over an extended array both in simulations and experiments at $V = 1\ \mu\text{m/s}$ (Fig. 3). In agreement with the experiments, the oscillation period in hexagonal arrays decreases with increasing velocity. Nonetheless, a discrepancy appears in the power law exponent, which we attribute to uncertainties on physical and/or control parameters. The nominal parameters that we use here give an onset velocity of morphological instability $V_c = DGk/[(k-1)mc_\infty] \approx 0.61\ \mu\text{m/s}$ for $G = 28$ K/cm, while V_c is lower since oscillating cells exist at $V = 0.5\ \mu\text{m/s}$ in the experiments. A set of parameters that reduces V_c to $0.35\ \mu\text{m/s}$ reproduces a scaling of $\tau(V)$, more consistent with the experiments (see Fig. 3). This supports our interpretation that the behavior $\tau \sim V^{-3/2}$ appears when V is sufficiently higher than V_c, since the oscillation period diverges as $V \longrightarrow V_c$. In addition, cell spacings tend to be shorter in simulations for estimated experimental values of G. We expect those discrepancies to be resolvable by a more accurate determination of physical and/or control parameters.

Additional simulations with larger box sizes containing up to 24 cells show that phase coherence is maintained spatiotemporally over the whole array when the initial condition corresponds to perfect hexagonal order. Those simulations further demonstrate that the lack of global coherence in experiments and simulations is linked to spatial disorder of the array. Spatial coherence is a comparatively longer range for confined thin-sample experiments that produce inherently ordered cellular or eutectic arrays [12,14,17–19]. Our results show that, even though local spatial ordering may lead to local coherence of oscillatory breathing modes, extended spatiotemporal coherence will generically not occur in a three-dimensional configuration. Without specific preparation of the initial state, both the intrinsic array dynamics and tip splitting promoted by cell oscillations maintain the array disorder, thereby inhibiting long-range phase coherence [31]. Those results highlight a rich interplay between array structure and dynamics in 3D.

N. B. and D. T. contributed equally to this work. This research was supported by CNES [Microstructures de Solidification 3D (MISOL3D) project] and NASA [Dynamical Selection of Interface Patterns (DSIP) project]. This work received support from the NASA Grants No. NNX07AK69G and No. NNX11AC09G, and from Région PACA [Étude Numérique et Expérimentale des Microstructures de Solidification (ENEMS) project].

---

[*] nathalie.bergeon@im2np.fr

[†] d.tourret@neu.edu

[1] M. C. Cross and H. Greenside, *Pattern Formation and Dynamics in Nonequilibrium Systems* (Cambridge University Press, Cambridge, England, 2009).

[2] W. Kurz and D. J. Fisher, *Fundamentals of Solidification* (Trans Tech Publications, Zurich, 1998), 4th ed.

[3] J. A. Dantzig and M. Rappaz, *Solidification* (EPFL Press, Lausanne, 2009).
[4] D. W. Thomson, *On Growth and Form* (Cambridge University Press, Cambridge, England, 1917).
[5] D. Weaire and N. Rivier, Contemp. Phys. **25**, 59 (1984).
[6] M. F. Miri and N. Rivier, Phys. Rev. E **73**, 031101 (2006).
[7] B. Billia and R. Trivedi, in *Handbook of Crystal Growth*, edited by D. T. J. Hurle (North-Holland, Amsterdam, 1993), Vol. 1b, Chap. 14, pp. 899–1073.
[8] H. Jamgotchian, N. Bergeon, D. Benielli, Ph. Voge, B. Billia, and R. Guérin, Phys. Rev. Lett. **87**, 166105 (2001).
[9] T. Schenk *et al.*, J. Cryst. Growth **275**, 201 (2005).
[10] K. Somboonsuk, J. T. Mason, and R. Trivedi, Metall. Trans. A **15**, 967 (1984).
[11] R. Trivedi and K. Somboonsuk, Acta Metall. **33**, 1061 (1985).
[12] P. E. Cladis, J. T. Gleeson, P. L. Finn, and H. R. Brand, Phys. Rev. Lett. **67**, 3239 (1991).
[13] S. Akamatsu, G. Faivre, and T. Ihle, Phys. Rev. E **51**, 4751 (1995).
[14] M. Georgelin and A. Pocheau, Phys. Rev. Lett. **79**, 2698 (1997).
[15] J. Deschamps, M. Georgelin, and A. Pocheau, Phys. Rev. E **78**, 011605 (2008).
[16] C. Misbah and A. Valance, Phys. Rev. E **49**, 166 (1994).
[17] B. Grossmann, K. R. Elder, M. Grant, and J. M. Kosterlitz, Phys. Rev. Lett. **71**, 3323 (1993).
[18] P. Kopczynski, W.-J. Rappel, and A. Karma, Phys. Rev. Lett. **77**, 3387 (1996).
[19] A. Karma and A. Sarkissian, Metall. Mater. Trans. A **27**, 635 (1996); M. Ginibre, S. Akamatsu, and G. Faivre, Phys. Rev. E **56**, 780 (1997).
[20] K. Kassner, J.-M. Debierre, B. Billia, N. Noël, and H. Jamgotchian, Phys. Rev. E **57**, 2849 (1998).
[21] M. Plapp and M. Dejmek, Europhys. Lett. **65**, 276 (2004).
[22] N. Bergeon, C. Weiss, N. Mangelinck-Noël, and B. Billia, Trans. Indian Inst. Metall. **62**, 455 (2009).
[23] N. Bergeon, A. Ramirez, L. Chen, B. Billia, J. Gu, and R. Trivedi, J. Mater. Sci. **46**, 6191 (2011).
[24] J. Teng and S. Liu, J. Cryst. Growth **290**, 248 (2006).
[25] S. Liu, J. Teng, and J. Choi, Metall. Mater. Trans. A **38**, 1555 (2007).
[26] See Supplemental Material at http://link.aps.org/supplemental/10.1103/PhysRevLett.110.226102 for videos of experiments [corresponding to Figs. 1(a), 1(b), and 2(a)] and simulations [Fig. 1(c)]; details of the phase-field model, simulation procedures, and computational parameters; and details of image post processing procedures for simulations and experiments.
[27] S. Gurevich, A. Karma, M. Plapp, and R. Trivedi, Phys. Rev. E **81**, 011603 (2010).
[28] A. Karma, Phys. Rev. Lett. **87**, 115701 (2001).
[29] B. Echebarria, R. Folch, A. Karma, and M. Plapp, Phys. Rev. E **70**, 061604 (2004).
[30] B. Echebarria, A. Karma, and S. Gurevich, Phys. Rev. E **81**, 021608 (2010).
[31] P. Cerisier, S. Rahal, and B. Billia, Phys. Rev. E **54**, 3508 (1996).